BIOCHEMISTRY
including biophysical chemistry & molecular biology
Article

Biochemistry **2010,** *49,* 10287–10297 10287
DOI: 10.1021/bi100500m

Intrinsically Disordered PEP-19 Confers Unique Dynamic Properties to Apo and Calcium Calmodulin†

Xu Wang, Quinn K. Kleerekoper, Liang-wen Xiong, and John A. Putkey*

Department of Biochemistry and Molecular Biology and Structural Biology Center, University of Texas, Houston Medical School, Houston, Texas 77030, United States

Received April 2, 2010; Revised Manuscript Received October 22, 2010

ABSTRACT: PEP-19 (Purkinje cell protein 4) is an intrinsically disordered protein with an IQ calmodulin (CaM) binding motif. Expression of PEP-19 was recently shown to protect cells from apoptosis and cell death due to Ca^{2+} overload. Our initial studies showed that PEP-19 causes novel and dramatic increases in the rates of association of Ca^{2+} with and dissociation of Ca^{2+} from the C-domain of CaM. The goal of this work was to study interactions between the C-domain of CaM (C-CaM) and PEP-19 by solution nuclear magnetic resonance (NMR) to identify mechanisms by which PEP-19 regulates binding of Ca^{2+} to CaM. Our results show that PEP-19 causes a greater structural change in apo C-CaM than in Ca^{2+}-C-CaM, and that the first Ca^{2+} binds preferentially to site IV in the presence of PEP-19 with exchange characteristics that are consistent with a decrease in Ca^{2+} binding cooperativity. Relatively weak binding of PEP-19 has distinct effects on chemical and conformational exchange on the microsecond to millisecond time scale. In apo C-CaM, PEP-19 binding causes a redistribution of residues that experience conformational exchange, leading to an increase in the number of residues around Ca^{2+} binding site IV that undergo conformational exchange on the microsecond to millisecond time scale. This appears to be caused by an allosteric effect because these residues are not localized to the PEP-19 binding site. In contrast, PEP-19 increases the number of residues that exhibit conformational exchange in Ca^{2+}-C-CaM. These residues are primarily localized to the PEP-19 binding site but also include Asp93 in site III. These results provide working models for the role of protein dynamics in the regulation of binding of Ca^{2+} to CaM by PEP-19.

PEP-19 (Purkinje cell protein 4) is a small 6.7 kDa polypeptide that was initially identified in the central nervous system (CNS) but is now known to be present in a variety of other tissues (for reviews, see refs (*1*−*5*)). PEP-19 has no known intrinsic activity other than binding to calmodulin (CaM)[1] in the presence or absence of Ca^{2+} via an IQ CaM binding motif. This gives PEP-19 the potential to exert broad cellular effects as a regulator of CaM signaling. This idea is consistent with a general cytoprotective role for PEP-19 put forth on the basis of the fact that Purkinje cells of the cerebellum and granule-cell neurons in the dentate gyrus, which have high levels of PEP-19, are largely spared from the effects of Alzheimer's disease, while PEP-19 negative cells are severely affected (*6*). Conversely, cell types that are most affected by Huntington's disease exhibit a significant loss of expression of PEP-19 (*7*). Experimental studies also support a cytoprotective role for PEP-19 because expression of PEP-19 greatly inhibits cell death due to apoptosis (*8*, *9*), or glutamate-induced Ca^{2+} cytotoxicity (*9*). Interestingly, the level of PEP-19 is greatly increased in human leiomyoma versus matched myometrium (*10*), and high levels of PEP-19 are found in 58 of 60 NCI-60 tumor cell lines (*11*), even cells derived from tissues that express low levels of PEP-19 or no PEP-19. This may be related to the increased survival potential of transformed cells due to the anti-apoptotic effects of PEP-19. These observations support the idea that PEP-19 protects cells against apoptosis and Ca^{2+} cytotoxicity because of normal or pathogenic conditions and would explain the need for high levels of PEP-19 in cells with highly active Ca^{2+} signaling systems.

The potential for PEP-19 to function as a regulator of CaM signaling led us to a series of studies to characterize its structural and biochemical properties, and its effects on CaM. We showed that PEP-19 binds relatively weakly but selectively to the C-domain of CaM and has novel effects on the Ca^{2+} binding properties of CaM (*12*). Specifically, PEP-19 causes a 40-fold increase in the rates of association (k_{on}) and dissociation (k_{off}) of Ca^{2+} at the C-domain of CaM, with little effect on Ca^{2+} binding affinity. Selective effects on the C-domain of CaM are important because the k_{on} and k_{off} for Ca^{2+} binding to the C-domain are up to 150-fold slower than for the N-domain and represent a rate-limiting step for activation of Ca^{2+}-dependent target proteins. We also showed that PEP-19 is intrinsically disordered, but with residual structure localized to an acidic/IQ motif that includes the

†This work was supported in part by training fellowships from the Keck Center Nanobiology Training Program of the Gulf Coast Consortia (National Institutes of Health Grant R90 DK071504) and the American Heart Association, South Central Affiliate (10POST3110010), and by grants from the Welch Foundation (AU-1144), the National Institutes of Health (R01 GM069611), and the American Heart Association, South Central Affiliate (GRNT2280427).

*To whom correspondence should be addressed: 6431 Fannin St., Houston, TX 77030. E-mail: john.putkey@uth.tmc.edu. Phone: (713) 500-6061. Fax: (713) 500-0652.

[1]Abbreviations: CaM, calmodulin; C-CaM, isolated C-domain of CaM; EDTA, 2,2′,2″,2‴-(ethane-1,2-diyldinitrilo)tetraacetic acid; EGTA, ethylene glycol bis(2-aminoethyl ether)-*N*,*N*,*N*′,*N*′-tetraacetic acid; HEDTA, *N*′-(2-hydroxyethyl)ethylenediamine-*N*,*N*,*N*′-triacetic acid; NTA, nitrilotriacetic acid; DSS, 2,2-dimethyl-2-silapentane-5-sulfonate; 3D, three-dimensional; HSQC, heteronuclear single-quantum coherence spectroscopy; R_1, longitudinal relaxation rate constant; R_2, transverse relaxation rate constant; NOE, nuclear Overhauser effect; SD, standard deviation; $\Delta\delta_{avg}$, average amide chemical shift change; τ_m, rotational correlation time; R_{ex}, chemical and conformational exchange; PDB, Protein Data Bank.

Published on Web 10/25/2010

IQ sequence and an adjacent acidic sequence (*13*). The core IQ motif is required for binding to CaM, but the acidic region is necessary to restrict binding to the C-domain, and for modulating binding of Ca^{2+} to CaM (*14*).

The C-domain of CaM has intriguing dynamic properties that may act in synergy with the intrinsic disorder of PEP-19. Protein dynamics from NMR showed that the C-domain of CaM presents an ensemble of conformational states. The "open" conformation is dominant in the presence of Ca^{2+} and the "closed" conformation in the apo state, but other minor populations of intermediate states exist (*15*−*17*). Akke and colleagues showed that the rate of Ca^{2+} exchange in the C-domain of CaM is correlated with rates of chemical and conformational exchange (*18*). Thus, binding targets to CaM provides a mechanism for altering its Ca^{2+} binding properties by changing its dynamic properties and the populations of CaM conformers. For example, binding high-affinity targets to Ca^{2+}-CaM shifts the conformational equilibrium by stabilizing an "open-like" Ca^{2+}-bound conformation, which greatly decreases k_{off} (*19*). On the basis of these observations, we propose an inverse mechanism in which low-affinity binding of intrinsically disordered PEP-19 modulates the slow dynamics of apo CaM and Ca^{2+}-bound CaM to increase Ca^{2+} binding rate constants.

This study provides experimental evidence to validate the hypothesis described above by investigating the effects of PEP-19 on the backbone dynamics of the isolated C-domain of CaM (C-CaM). In contrast to high-affinity binding peptides, association of PEP-19 with CaM alters conformational exchange on the microsecond to millisecond timescale. Specifically, binding PEP-19 to apo C-CaM redistributes residues that experience conformational exchange, with a significant number localized to Ca^{2+}-binding site IV. Binding PEP-19 to Ca^{2+}-bound C-CaM increases the number of residues that exhibit conformational exchange, especially those in the linker between helices F and G. This provides working models for the structural and dynamic basis for the effect of PEP-19 on the kinetics of binding of Ca^{2+} to CaM.

MATERIALS AND METHODS

Protein Purification. Recombinant CaM and PEP-19 were cloned, expressed in bacteria, and purified as described previously (*12*, *13*, *20*, *21*). A bacterial expression vector for C-CaM (residues 76−148) was kindly provided by M. Shea (University of Iowa, Iowa City, IA). Proteins were decalcified by addition of 5 mM EGTA and 0.1 mM BAPTA followed by desalting on a Bio-Rad P6DG or P2DG size exclusion column into a buffer that was decalcified by passage over a calcium-sponge column (Molecular Probes). Protein concentrations were estimated using extinction coefficients (ε_{276} = 0.18 mL^{-1} mg^{-1} for CaM, and ε_{215} = 0.115 mL^{-1} mg^{-1} for PEP-19) or by using the BCA protein assay (Pierce). More precise concentrations of CaM and C-CaM were determined by measuring the amount of Ca^{2+} released from the C-domain of Ca^{2+}-saturated proteins. Briefly, a solution of approximately 2 μM CaM or C-CaM and 30 μM Ca^{2+} was rapidly mixed with a solution of the Ca^{2+} sensitive dye, Quin-2 (at 300 μM), using a stopped flow fluorimeter to monitor the slow release of Ca^{2+} from the C-domain as described previously (*12*). The amount of Ca^{2+} released from the sample was determined by calibrating the fluorescence response with EGTA standards. This was then used to calculate the concentration of CaM or C-CaM.

Equilibrium Ca^{2+} Titrations Monitored by Tyrosine Fluorescence. Equilibrium Ca^{2+} binding constants for CaM and C-CaM in the presecnce or absence of PEP-19 were determined using tryosine fluoresence as described previously (*22*). Solutions containing 20 mM MOPS (pH 7.5), 100 mM KCl, 1 mM EGTA, 1 mM HEDTA, 1 mM NTA, and 5 μM CaM or C-CaM with or without 30 μM PEP-19 were titrated with a Ca^{2+} stock to achieve a wide range of free Ca^{2+} concentrations. The concentration of total Ca^{2+} needed to achieve a desired free Ca^{2+} concentration was determined using the online calculator MaxChelator (http://www.stanford.edu/~cpatton/maxc.html). The Ca^{2+} stock was prepared in the same buffer, including proteins, such that only the concentration of Ca^{2+} was changed during the titration. Tyrosine fluorescence intensity was plotted against the free Ca^{2+} concentration and fit to the following form of the Hill equation:

$$F = F_{min} + (F_{max} - F_{min})\left(\frac{[Ca]^n}{[Ca]^n + k_{Ca}{}^n}\right) \quad (1)$$

where $[Ca^{2+}]$ is the free Ca^{2+} concentration, F is the fluorescence intensity at a given free Ca^{2+} concentration, F_{min} is the initial fluorescence intensity in the absence of added Ca^{2+}, F_{max} is the fluorescence at the maximal Ca^{2+} concentration, k_{Ca} is the concentration of Ca^{2+} at which the change in fluorescence is half-maximal, and n is the Hill coefficient.

NMR Methodology. All NMR experiments were performed on a Bruker DRX 600 MHz spectrometer equipped with a 5 mm triple-resonance cryoprobe at 298 K. NMR samples were prepared using decalcified proteins in a buffer containing 10 mM imidazole, 100 mM KCl, and 5% D_2O (pH 6.3). Samples used for relaxation measurements and backbone assignments contained 0.5 mM C-CaM uniformly labeled with ^{15}N or with ^{13}C and ^{15}N, with or without 0.7 mM PEP-19. Excess EDTA or $CaCl_2$ was added to maintain the apo or Ca^{2+}-bound state, respectively.

Backbone assignments for the C-CaM−PEP-19 complex for apo and Ca^{2+}-bound states were obtained using the following 3D experiments: HNCO, HNCA, HN(CO)CA, HNCACB, CBCA-(CO)NH, ^{15}N HSQC-TOCSY, and ^{15}N-edited NOESY-HSQC. The ^{15}N longitudinal (R_1) and transverse (R_2) relaxation rate constants and heteronuclear $^1H-^{15}N$ NOE values were acquired using published pulse sequences (*23*). Experiments were conducted with delays of 20, 100, 200, 400, 600, 800, 1000, 1200, and 1400 ms for R_1 measurements and delays of 16.96, 33.92, 50.88, 67.84, 84.8, 118.72, 135.68, 152.64, and 169.6 ms for R_2 measurements. $^1H-^{15}N$ NOE values were measured from spectra with and without proton saturation recorded in an interleaved manner. Proton saturation was acquired using a 120° ^1H pulse applied every 5.0 s. In the case of the NONOE spectra, a net relaxation delay of 5.0 s was employed, while a relaxation delay of 2.0 s prior to a 3.0 s proton presaturation period was employed for the NOE spectra.

All NMR spectra were processed and analyzed using Topspin 2.0 (Bruker) and FELIX 2004 (MSI, San Diego, CA). ^1H chemical shifts were referenced to DSS (2,2-dimethyl-2-silapentane-5-sulfonate), and ^{15}N and ^{13}C chemical shifts were referenced indirectly using their respective gyromagnetic ratios (*24*). The average amide chemical shift change ($\Delta\delta_{avg}$) was calculated using the following equation:

$$\Delta\delta_{avg} = \sqrt{\frac{(\Delta\delta H)^2 + (\Delta\delta N/5)^2}{2}} \quad (2)$$

where $\Delta\delta H$ and $\Delta\delta N$ are the changes in ^1H and ^{15}N chemical shifts, respectively.

Analysis of Relaxation Data. Values for R_1, R_2, and their uncertainties were derived by plotting peak intensity versus delay time and fitting the data to a single-exponential decay equation using nonlinear least-squares analysis. $^1H-^{15}N$ NOE values were calculated from the ratios of peak intensities with and without presaturation. The standard deviation of the NOE was calculated from the root-mean-square value of the background noise in the spectra (*23*).

Reduced spectral density mapping was used to analyze the relaxation data (*25*, *26*). Values for $J(0)$, $J(\omega_N)$, and $J(\omega_H)$ were derived from

$$J(\omega_H) \approx J(\omega_H + \omega_N) \approx J(\omega_H - \omega_N) \quad (3)$$

$$R_{NOE} = (NOE - 1)R_1(\gamma_N/\gamma_H) \quad (4)$$

$$J(0) = (-0.75R_1 + 1.5R_2 - 0.9R_{NOE})/E \quad (5)$$

$$J(\omega_N) = (R_1 - 1.4R_{NOE})/E \quad (6)$$

$$J(\omega_H) = R_{NOE}/5A \quad (7)$$

where

$$E = 3A + C^2$$

$$A = (\mu_0 h\gamma_H\gamma_N/16\pi^2 r_{NH}{}^3)^2$$

$$C = (\omega_N/\sqrt{3})(\sigma_{||} - \sigma_\perp)$$

where μ_0 is the permeability of free space, h is Planck's constant, γ_H and γ_N are the gyromagnetic ratios of ^1H and ^{15}N, respectively, and r_{NH} is the average N−H bond length (1.02 Å). Uncertainties in the spectral density parameters were estimated using 500 Monte Carlo simulations based on the uncertainties in the measured relaxation parameters.

Residue-specific rotational correlation times (τ_m) were estimated from the R_2/R_1 ratio (*27*) (software r2r1_tm, A. G. Palmer, III, Columbia University, New York, NY). Residues with R_2/R_1 ratios falling outside one standard deviation (SD) of the mean, as well as residues with NOE values of < 0.65, were excluded from the analysis (*28*).

RESULTS

C-CaM Is a Valid Structural Model for Studying Interactions between CaM and PEP-19. We showed previously that application of NMR to study the interactions between PEP-19 and apo CaM was severely limited because resonances for most backbone amides were broadened beyond detection in the apo CaM−PEP-19 complex (*13*). This was not due to the interaction of PEP-19 with the N-domain of CaM because amide chemical shifts in the N-domain are unaffected by PEP-19 binding (see Figure 1 of the Supporting Information). We felt that use of the isolated C-CaM may overcome this limitation because of the different rotational correlation times or other factors relative to intact CaM. This strategy was justified on the basis of previous studies showing that the isolated C-CaM retains the biochemical properties of the intact protein (*29*−*32*). In addition, we showed that PEP-19 binds preferentially to the C-domain of CaM in the absence or presence of Ca^{2+} and that PEP-19 has the same effects on the Ca^{2+} k_{off} rate of both C-CaM and intact CaM (*13*, *14*). Thus, the initial goal of this study was to determine if amide resonances in apo C-CaM can be observed upon binding PEP-19. Indeed, addition of PEP-19 to apo C-CaM allows observation of slow, two-state exchange for most amides. Backbone assignments for apo C-CaM bound to PEP-19 were obtained by HNCA, HN(CO)CA, HNCACB, CBCA(CO)NH, ^{15}N HSQC-TOCSY, and ^{15}N-edited NOESY-HSQC experiments. All backbone amides were assigned except for Asp131 and Gly134, which are undetectable because of line broadening.

We next determined if C-CaM provided a good structural mimic of the C-domain from intact CaM in the absence of PEP-19. Figure 2 of the Supporting Information compares the $^1H-^{15}N$ HSQC spectra of C-CaM versus intact CaM in the presence and absence of Ca^{2+}. The spectra of C-CaM are greatly simplified due to the absence of amide cross-peaks from residues in the N-domain of CaM. As expected, amide chemical shifts for residues at the N-terminus of C-CaM, including the N-terminal portion of helix E, exhibit greater average amide chemical shift differences ($\Delta\delta_{avg}$) relative to CaM because of the lack of influence from the tethered N-domain (see Figure 3 of the Supporting Information). However, average $\Delta\delta_{avg}$ values for residues 88−148 of C-CaM and intact CaM are 0.014 and 0.012 in the absence and presence of Ca^{2+}, respectively, which are within the error of these measurements and calculations. In addition, the secondary structures of C-CaM and the C-domain of intact CaM are in excellent agreement in the presence and absence of Ca^{2+} as determined by $^{13}C_\alpha$ secondary chemical shifts, $^1H-^{15}N$ NOESY-HSQC, $^3J_{HAHA}$, and the chemical shift index (see Table 1 of the Supporting Information).

We next compared $^1H-^{15}N$ HSQC spectra for Ca^{2+}-bound C-CaM and intact CaM at increasing concentrations of PEP-19 at 298 K. Residues in the N-domain of CaM are not affected by PEP-19 binding, and most resonances in Ca^{2+}-bound C-CaM exhibit characteristics of fast to intermediate exchange when titrated with PEP-19. This allows the assignment of backbone amides by following the movement of cross-peaks. Assignments were then verified by $^1H-^{15}N$ NOESY-HSQC. All residues were assigned except for Thr110, Asn111, Gly113, Glu114, and Lys115, due to severe resonance line broadening. Figure 4 of the Supporting Information shows that all amide cross-peaks for Ca^{2+}-C-CaM bound to PEP-19 superimpose on resonances associated with the C-domain of intact CaM bound to PEP-19 except residues 78−82 at the N-terminus of C-CaM. Thus, binding PEP-19 induces similar conformations in the Ca^{2+}-bound forms of both C-CaM and the C-domain of intact CaM. Together, Figures 1−4 of the Supporting Information demonstrate that C-CaM is a valid structural model for the study of interactions between CaM and PEP-19 in the presence or absence of Ca^{2+}.

Characteristics of slow and fast exchange on the NMR time scale for C-CaM amide resonances during titration with PEP-19 in the absence and presence of Ca^{2+}, respectively, are consistent with the kinetics of binding PEP-19. Observed exchange characteristics are dependent on the relationship between chemical exchange (k_{ex}) and the difference in frequency for amide resonances between the bound and free states ($\Delta\omega$). Fast exchange is observed if $k_{ex} > \Delta\omega$, while slow exchange is seen if $k_{ex} < \Delta\omega$. On this basis, we can conclude that $k_{ex} > 150\ s^{-1}$ in the presence of Ca^{2+} and $k_{ex} < 20\ s^{-1}$ in the absence of Ca^{2+}. The k_{ex} will be largely determined by k_{off} during the titration of C-CaM with PEP-19 because $k_{ex} = [\text{PEP-19}]_{free}k_{on} + k_{off}$, and $[\text{PEP-19}]_{free}$ will be very low until its total level exceeds that of C-CaM in the NMR sample. Thus, the above partial limits of k_{ex} based on $\Delta\omega$ are reasonable because we know that k_{off} values are 400 and 5 s^{-1}

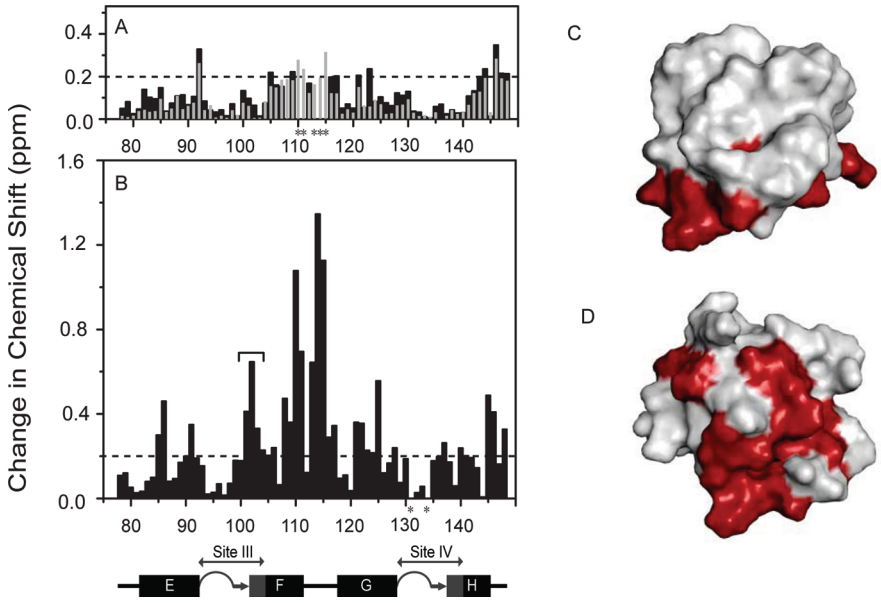

FIGURE 1: Effects of PEP-19 on C-CaM amides in the absence and presence of Ca^{2+}. (A) Amide chemical shift perturbations ($\Delta\delta_{avg}$) for Ca^{2+}-bound C-CaM at 298 K are shown as black bars. Gray bars show $\Delta\delta_{avg}$ values that result from binding of PEP-19 to the C-domain of intact Ca^{2+}-CaM at 320 K (*14*). Asterisks denote resonances with significant line broadening in the presence of PEP-19. (B) $\Delta\delta_{avg}$ values for apo C-CaM at 298 K. Panels C and D map residues with $\Delta\delta_{avg}$ values of > 0.2 ppm on the solvent accessible surfaces of Ca^{2+}-C-CaM (PDB entry 1J7P) and apo C-CaM (PDB entry 1F71), respectively. The structures are presented in the same relative orientation. The diagram below panel B shows the relative positions of helices E−H in the primary sequence of CaM. The 12 amino acids of Ca^{2+} binding sites III and IV are also colored gray. Coil, β-strand, and α-helical portions of these structures are indicated by loops, arrows, and boxes, respectively.

for binding PEP-19 to CaM in the presence and absence of Ca^{2+}, respectively (*13*, *14*).

PEP-19 Has a Stronger Effect on the Structure of Apo versus Ca^{2+}-Bound C-CaM. Black bars in Figure 1A show that binding of PEP-19 yields relatively small $\Delta\delta_{avg}$ values in Ca^{2+}-C-CaM at 298 K (see Figure 5A of the Supporting Information for complete spectra). The largest values of $\Delta\delta_{avg}$ are seen for residues Met144−Lys148 at the C-terminus, while amide resonances for residues Thr110−Lys115 in the linker between sites III and IV are broadened beyond detection upon binding PEP-19. Experiments performed previously at 320 K with intact Ca^{2+}-CaM (*14*) showed very similar patterns of $\Delta\delta_{avg}$ (see the gray bars in Figure 1A), except that resonances for residues Thr110−Lys115 were observed. This temperature dependence indicates that significant conformational exchange occurs on the microsecond to millisecond time scale for residues at the end of helix F and the linker between helices F and G of Ca^{2+}-CaM when bound to PEP-19.

Figure 1B shows that binding PEP-19 causes much greater $\Delta\delta_{avg}$ values in apo C-CaM than in Ca^{2+}-bound C-CaM. Similar to Ca^{2+}-C-CaM, residues with the largest $\Delta\delta_{avg}$ values in apo C-CaM are localized to helix F and the linker between helices F and G, but changes are also seen for residues 101−103 at the transition between β-strand and helical structures in Ca^{2+} binding site III. Panels C and D of Figure 1 illustrate the binding interface between C-CaM and PEP-19 in the absence and presence of Ca^{2+} based on residues with $\Delta\delta_{avg}$ values of > 0.2 ppm.

Experiments were performed to determine if apo and Ca^{2+}-bound C-CaM have different secondary structures when bound to PEP-19 that could account for different magnitudes and patterns of chemical shift changes in panels A and B of Figure 1. Figure 6 and Table 1 of the Supporting Information show that secondary structures in the C-domain of CaM are essentially identical in the presence and absence of Ca^{2+} or PEP-19. Moreover, the antiparallel β-sheet between loops III and IV in apo and Ca^{2+}-bound C-CaM remains intact when bound to PEP-19 on the basis of the presence of long-range NOE values (d_{NN}) between Ile100 and Val136 (data not shown). The largest difference in secondary structure is observed for helix F, which terminates at Val108 in apo C-CaM when bound to PEP-19 but extends to Asn111 under all other conditions. These data, together with Figure 1, suggest that Ca^{2+}-bound C-CaM remains predominantly in an open-like conformation in the presence of PEP-19 but that binding PEP-19 may alter interhelical angles in apo C-CaM.

Effect of PEP-19 on the Ca^{2+} Binding Cooperativity of C-CaM. We showed previously that PEP-19 increased Ca^{2+} k_{off} and k_{on} rates and decreased the cooperativity of Ca^{2+} binding to the C-domain of intact CaM without greatly affecting the K_d (*14*). Specifically, the macroscopic Ca^{2+} dissociation constants for the C-domain of CaM are as follows: $K_{d1} = 17\,\mu$M, and $K_{d2} = 0.4\,\mu$M. This indicates positive cooperativity because $K_{d1} > 4K_{d2}$, with a change in free energy due to cooperativity ($\Delta\Delta G_c$) of −3.4 kcal/mol. In the presence of PEP-19, $K_{d1} = 4.7\,\mu$M and $K_{d2} = 2.0\,\mu$M, which demonstrates a significant loss of cooperativity, with a $\Delta\Delta G_c$ of −1.3 kcal/mol. Despite these changes in macroscopic binding constants and cooperativity, the overall K_d values for the binding of Ca^{2+} to the C-domain are very similar in the presence or absence of PEP-19. We also showed that PEP-19 increased the Ca^{2+} k_{off} rate of isolated C-CaM (*14*). Figure 2 uses fluorescence from Tyr99 and Tyr138 to show that PEP-19 also decreases the cooperativity of binding of Ca^{2+} to C-CaM as indicated by a decreased Hill coefficient in the presence of PEP-19 but does not greatly affect the K_d for Ca^{2+} binding. Thus, the effects of PEP-19 on the C-domain of intact CaM are also seen for C-CaM.

To identify potential structural manifestations of decreased cooperativity, we monitored amide chemical shifts by a series of $^1H-^{15}N$ HSQC spectra collected during titration of C-CaM with Ca^{2+} in the absence or presence of PEP-19 at 298 K. Figure 3 uses

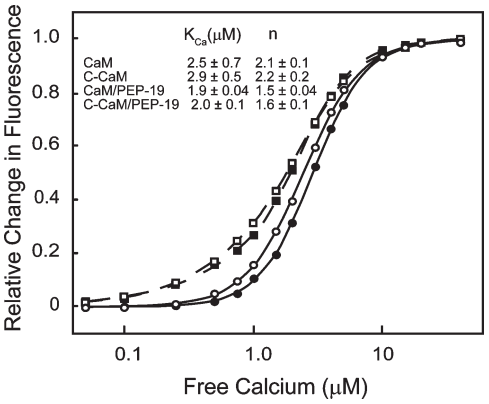

FIGURE 2: Effect of PEP-19 on the Ca^{2+} binding constant (K_{ca}) and Hill coefficient (n). Intrinsic tyrosine fluorescence was monitored during titration of CaM (○), the CaM−PEP-19 complex (□), C-CaM (●), and the C-CaM−PEP-19 complex (■) with Ca^{2+}. The lines show fits of the data to the Hill equation (eq 1).

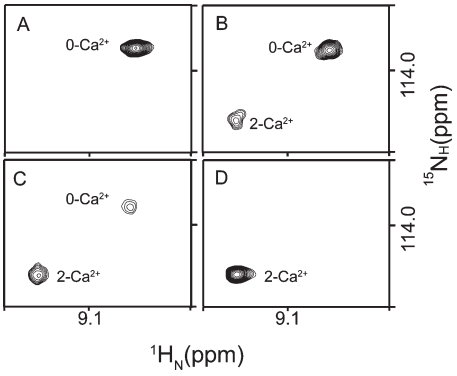

FIGURE 3: Ca^{2+}-dependent changes in amide chemical shifts of C-CaM show strong cooperativity. The resonance of Thr117 in the linker region of C-CaM exhibits two-state slow exchange at various molar ratios of Ca^{2+} to C-CaM, indicating highly cooperative binding of Ca^{2+} to sites III and IV: (A) [Ca^{2+}]/[C-CaM] = 0, (B) [Ca^{2+}]/[C-CaM] = 0.3, (C) [Ca^{2+}]/[C-CaM] = 0.6, and (D) [Ca^{2+}]/[C-CaM] = 2.0.

Thr117 to demonstrate slow two-state exchange observed for amide resonances in the absence of PEP-19. At intermediate levels of Ca^{2+} (Figure 3B,C), resonances for both zero-Ca^{2+} and two-Ca^{2+} forms are observed with relative intensities that are proportional to their populations. No evidence of the one-Ca^{2+} form is observed at intermediate Ca^{2+} levels in the absence of PEP-19, indicating highly cooperative Ca^{2+} binding.

Figure 4 shows that fast to intermediate exchange on the NMR chemical time scale is observed upon titration of C-CaM with Ca^{2+} in the presence of PEP-19. Peaks corresponding to residues in Ca^{2+} binding sites III and IV and helices E and F have large Ca^{2+}-dependent changes in amide chemical shifts that could not be detected at intermediate Ca^{2+} titration points because of line broadening. However, residues such as Thr117 that experience smaller overall Ca^{2+}-dependent amide chemical shift changes could be observed at all Ca^{2+} levels. The NMR spectral characteristics of Thr117 in Figure 4A show resonance line broadening and splitting into multiple peaks at low Ca^{2+} levels, indicating rapid exchange between multiple conformations. Moreover, during titration with Ca^{2+}, Thr117 exhibits a biphasic change with an upfield shift in the ^1H dimension between Ca^{2+}:C-CaM ratios of 0 and 1.0, and then a downfield shift in the ^{15}N dimension at Ca^{2+}:C-CaM ratios between 1.0 and 2.0. These data are consistent with decreased cooperativity for binding of Ca^{2+} in

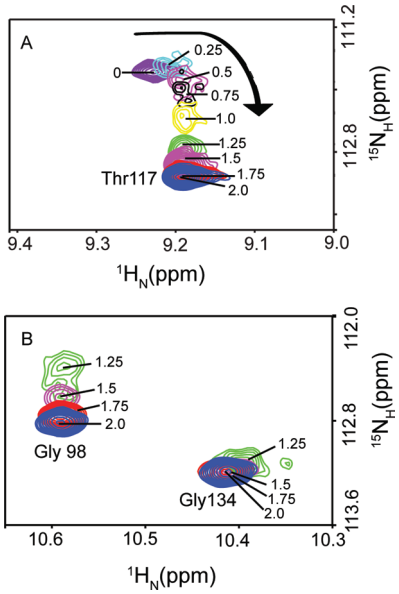

FIGURE 4: Ca^{2+}-dependent changes in amide chemical shifts of C-CaM in the presence of PEP-19 show decreased cooperativity. Various [Ca^{2+}]/[C-CaM] ratios between 0 and 2.0 are indicated. Exchange characteristics for Thr117 shown in panel A indicate a lower degree of cooperativity for binding of Ca^{2+} in the presence of PEP-19. Exchange characteristics for Gly98 in Ca^{2+} binding site III and Gly134 in Ca^{2+} binding site IV shown in panel B, which indicates preferential binding of the first Ca^{2+} to site IV.

the presence of PEP-19 that results in significant populations of the one-Ca^{2+} form of C-CaM at substoichiometric levels of Ca^{2+}.

Gly98 and Gly134 at position 6 of loops III and IV, respectively, were selected to provide information about the sequential nature of binding of Ca^{2+} to C-CaM in the presence of PEP-19. These glycines provide markers for Ca^{2+} binding because they facilitate the unusual main chain conformation that allows the Ca^{2+} ligands to take up coordinating positions (*33*). The large differences in amide chemical shifts of Gly98 and Gly134 between apo and Ca^{2+}-bound forms lead to severe resonance broadening at intermediate Ca^{2+} levels. However, Figure 4B shows that the change in chemical shift for Gly134 is maximal at a Ca^{2+}:C-CaM ratio of around 1.0, while the change in chemical shift for Gly98 is not maximal until a Ca^{2+}:C-CaM ratio of 2.0 is reached. These data indicate that PEP-19 promotes preferential binding of the first Ca^{2+} to site IV. However, Figure 4B shows that Gly98 in site III experiences a minor conformational change upon binding the first Ca^{2+} to site IV, and binding the second Ca^{2+} to site III sharpens the line width of Gly134 in site IV. The simplest interpretation of these data is that PEP-19 decreases but does not eliminate cooperativity between sites III and IV.

Effects of PEP-19 on the Backbone Dynamics of C-CaM. To improve our understanding of the effects of PEP-19 on backbone dynamics in C-CaM, ^{15}N relaxation experiments for apo and Ca^{2+}-bound C-CaM were conducted in the absence or presence of PEP-19. The $^1H-^{15}N$ NOE is typically most sensitive to motions on the picosecond to nanosecond time scale, with values near 1.0 indicating a lack of such motions, and lower values indicating increasing local flexibility of the polypeptide. As in previous reports (*15*, *17*, *34*), panels A and F of Figure 5 show significant reductions in NOE values for residues at the N- and C-termini of C-CaM in the presence or absence of Ca^{2+}. The two Ca^{2+} binding loops and the linker between helix F and helix G also show lower NOE values. Binding PEP-19 had no significant

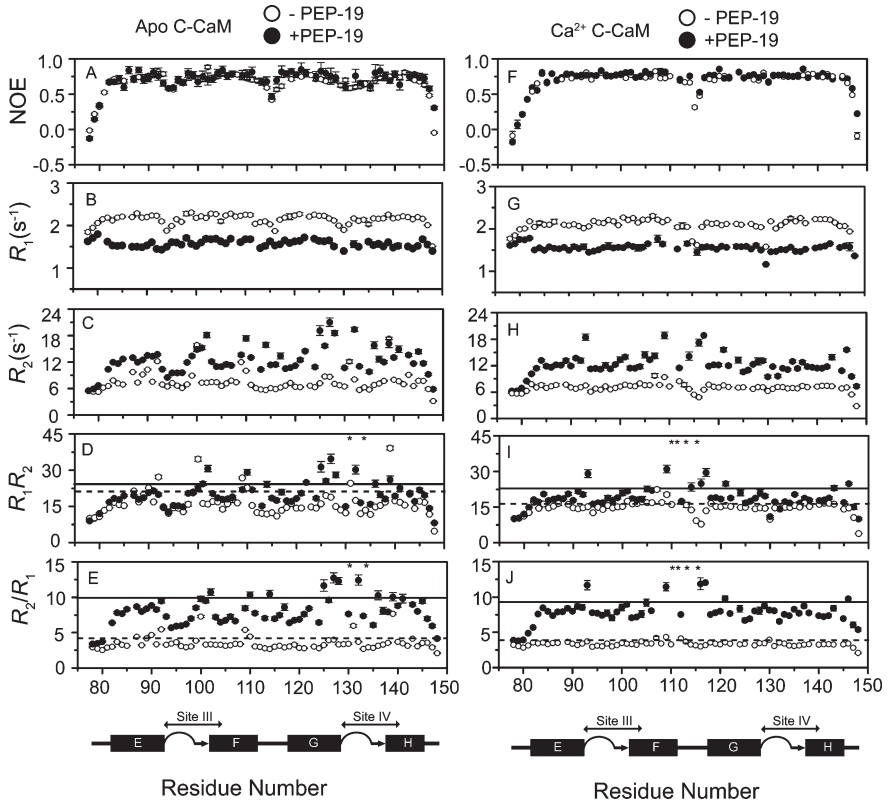

FIGURE 5: Backbone ^{15}N relaxation parameters for apo C-CaM, the apo C-CaM−PEP-19 complex, Ca^{2+}-bound C-CaM, and the Ca^{2+}-bound C-CaM−PEP-19 complex. R_1, R_2, and $^1H-^{15}N$ NOE values, R_2R_1 products, and R_2/R_1 ratios are shown for apo and Ca^{2+}-bound C-CaM in the absence (○) and presence (●) of PEP-19. The dashed (without PEP-19) and solid (with PEP-19) lines in panels C, D, G, and H indicate the mean ± one standard deviation. Asterisks denote resonances with significant line broadening in the presence of PEP-19.

Table 1: Summary of R_1, R_2, NOE, R_1R_2, R_2/R_1, τ_m, $J(0)$, $J(\omega_N)$, and $J(\omega_H)$ Values

	^{15}N relaxation parameters						reduced spectral density mapping		
protein	R_1 (s^{-1})	R_2 (s^{-1})	NOE	R_1R_2	R_2/R_1	τ_m (ns)	$J(0)$ (ns/rad)	$J(\omega_N)$ (ns/rad)	$J(\omega_H)$ (ns/rad)
apo C-CaM	2.14 ± 0.13	7.6 ± 2.2	0.67 ± 0.16	16.3 ± 5.2	3.51 ± 0.96	4.83 ± 0.46	1.88 ± 0.64	0.40 ± 0.03	0.011 ± 0.004
apo C-CaM−PEP-19	1.58 ± 0.085	12.5 ± 3.2	0.70 ± 0.17	19.7 ± 5.2	7.93 ± 2.00	8.33 ± 0.66	3.40 ± 0.92	0.29 ± 0.017	0.008 ± 0.004
Ca^{2+}-C-CaM	2.09 ± 0.17	7.1 ± 1.0	0.68 ± 0.19	14.8 ± 2.7	3.36 ± 0.33	4.81 ± 0.19	1.74 ± 0.26	0.39 ± 0.04	0.010 ± 0.005
Ca^{2+}-C-CaM−PEP-19	1.56 ± 0.091	12.2 ± 2.5	0.70 ± 0.18	18.9 ± 4.1	7.82 ± 1.60	8.38 ± 0.37	3.08 ± 0.79	0.29 ± 0.014	0.009 ± 0.007

effect on NOE values for apo or Ca^{2+}-bound C-CaM (see Table 1). This confirms the results in Table 1 of the Supporting Information showing that C-CaM−PEP-19 complexes have well-defined secondary structures.

Figure 5 and Table 1 show that binding of PEP-19 to C-CaM causes an overall decrease in R_1, and an increase in R_2 in the presence or absence of Ca^{2+}. A molecular rotational correlation time (τ_m) of 4.8 ns is estimated from R_2/R_1 ratios for free apo and Ca^{2+}-bound C-CaM (see Table 1). This is consistent with the τ_m of 4.9 ns determined by Malmendal et al. (*15*) for apo C-CaM using the mean η_{xy}/η_z ratio and Model-Free analysis. The estimated τ_m for C-CaM is increased to 8.3 ns when it is bound to PEP-19 in the presence or absence of Ca^{2+}. The τ_m ratio of 1.73 for the C-CaM−PEP-19 complex versus free C-CaM is comparable to their molecular weight ratio of 1.77, which suggests that the complexes are close to globular in shape. Residues with unusually high R_2/R_1 ratios relative to the average indicate regions that undergo conformational exchange processes on the microsecond to millisecond time scale (*35*). The R_1R_2 product is an effective discriminator of motional anisotropy and chemical and conformational exchange (*36*). Panels D and I of Figure 5 show the R_2R_1 product and panels E and J of Figure 5the R_2/R_1 ratios for residues in apo and Ca^{2+}-bound C-CaM in the presence and absence of PEP-19. Table 2 lists residues with R_2/R_1 and R_1R_2 values that are both greater than one standard deviation relative to the average.

The Model-Free approach to predict residues with R_{ex} was not used because 3D structures of C-CaM−PEP-19 complexes are not available, and isotropic conditions cannot be assumed. Instead, the relaxation data were further analyzed using reduced spectral density mapping. The advantage of this approach lies in the absence of assumptions made a priori regarding internal motions and molecular tumbling (*25*, *26*). Reduced spectral density mapping assumes that the high-frequency spectral density terms are approximately equal in magnitude [i.e., $J(\omega_H \pm \omega_N) \approx J(\omega_H)$] and therefore may be replaced by a single value, $J(\omega_H)$. Reduced spectral density terms $J(\omega_H)$, $J(\omega_N)$, and $J(0)$ were calculated according to eqs 3−7 (see Materials and Methods) for apo and Ca^{2+}-bound C-CaM in the presence and absence of PEP-19, as summarized in Table 1 and Figure 6. $J(\omega_H)$ is correlated with fast internal motion of N−H bond vectors on the picosecond to nanosecond time scale. Because the value of the

Table 2: Summary of Residues That Undergo Conformational Exchange on the Microsecond to Millisecond Time Scale[a]

protein	R_2/R_1		R_2R_1		reduced spectral density mapping		exchange broadening	
apo C-CaM	**Glu87**	**Met109**	**Glu87**	**Met109**	**Glu87**	**Met109**		
	Arg90	**Thr110**	**Arg90**	**Thr110**	**Arg90**	**Thr110**		
	Phe92	**Asp131**	**Phe92**	**Asp131**	**Phe92**	**Asp131**		
	Ile100	**Glu139**	**Ile100**	**Glu139**	**Ile100**	**Glu139**		
apo C-CaM−PEP-19	**Ala102**	**Ala128**	Ala102	Glu127	Ala102	Ala128	**Asp131**	
	Thr110	**Gly132**	**Thr110**	**Ala128**	**Thr110**	**Gly132**	**Gly134**	
	Glu114	**Val136**	**Glu114**	**Gly132**	**Glu114**	**Val136**		
	Ile125	**Glu139**	**Asp122**	**Val136**	**Ile125**	**Glu139**		
	Glu127		**Ile125**	**Glu139**	**Glu127**			
			Arg126					
Ca^{2+}-C-CaM	Asp93	**Leu112**	Ser101	**Met109**	**Glu104**	**Leu112**		
	Glu104	Gly113	**Glu104**	**Leu112**	**His107**	**Met 109**		
	His107	Ile130	**His107**					
	Met109							
Ca^{2+}-C-CaM−PEP-19	**Asp93**	**Thr117**	**Asp93**	**Val121**	**Asp93**	**Thr117**	**Thr 110**	**Glu114**
	Met109	**Val121**	**Met109**	Gln143	**Met109**	**Val121**	**Asn111**	**Lys115**
	Leu116	**Thr146**	**Leu116**	**Thr146**	**Leu116**	**Thr146**	**Gly 113**	
			Thr117					

[a]Residues that exhibit conformational exchange by all criteria are shown in bold.

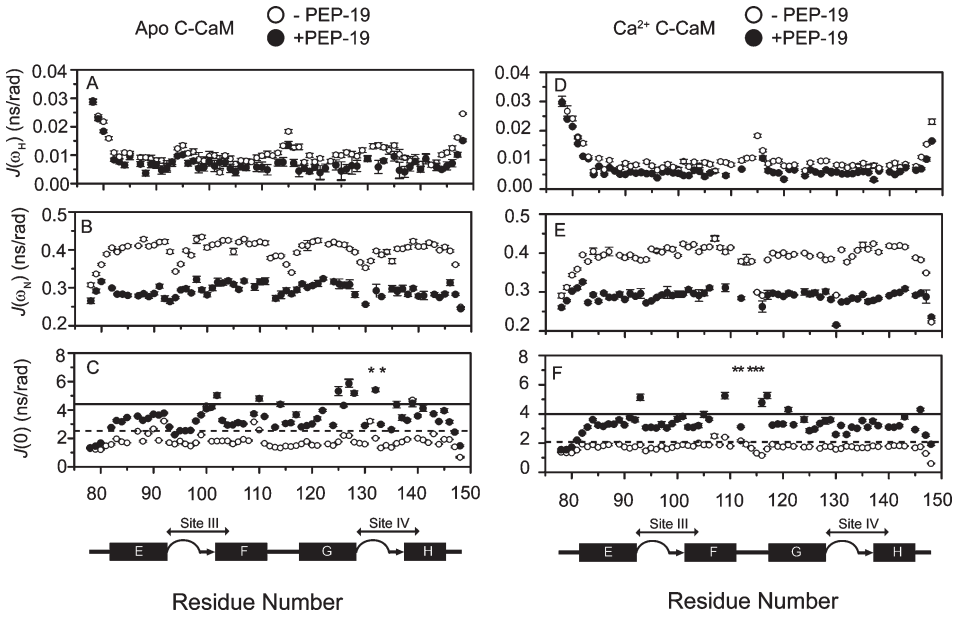

FIGURE 6: Reduced spectral density mapping for apo C-CaM, the apo C-CaM−PEP-19 complex, Ca^{2+}-C-CaM, and the Ca^{2+}-C-CaM−PEP-19 complex. Reduced spectral density parameters were calculated using eqs 3−7. $J(\omega_H)$, $J(\omega_N)$, and $J(0)$ are shown for apo and Ca^{2+}-bound C-CaM in the absence (○) and presence (●) of PEP-19. The mean ± one standard deviation of $J(0)$ for apo and Ca^{2+}-bound C-CaM in the absence and presence of PEP-19 is indicated by dashed and solid lines, respectively. Asterisks denote resonances with significant line broadening in the presence of PEP-19.

area under the $J(\omega)$ curve is constant, highly flexible segments of the backbone are characterized by high $J(\omega_H)$ values and low $J(0)$ and $J(\omega_N)$ values. This is observed for the N- and C-termini and the linker between helices F and G of C-CaM. Panels A and D of Figure 6 show that PEP-19 has relatively little effect on $J(\omega_H)$ for residues in C-CaM in the presence or absence of Ca^{2+}. This indicates little effect of PEP-19 on the backbone dynamics of C-CaM on the picosecond to nanosecond time scale and is consistent with the lack of an effect of PEP-19 on heteronuclear NOEs.

An increase in molecular mass due to complex formation will globally increase $J(0)$; however, residues with unusually high $J(0)$ values relative to the average in a given protein or complex indicate significant chemical and conformational exchange on the microsecond to millisecond time scale due to contributions from R_{ex} on R_2 (*25*, *26*, *37*). Figure 7 shows residues in C-CaM with $J(0)$ values that are increased relative to the average $J(0)$ based on the expression $[J(0) - J(0)_{avg}]/SD$. For example, Figure 7A shows that $J(0)$ values are increased by more than one standard deviation relative to $J(0)_{avg}$ for Arg90, Phe92, Tyr99, Ile100, Thr110, Asp131, and Glu139. These same residues were shown by Malmendal et al. (*15*) to have the greatest R_{ex} on the basis of Model-Free analysis. Interestingly, Figure 7 shows that binding PEP-19 causes large variations in $J(0)$ for residues in C-CaM in the presence or absence of Ca^{2+}. Residues in Table 2 that are highlighted in bold exhibit conformational exchange based on severe line width broadening, or $J(0)$, R_2/R_1, and R_1R_2 values that are all more than one standard deviation from the average.

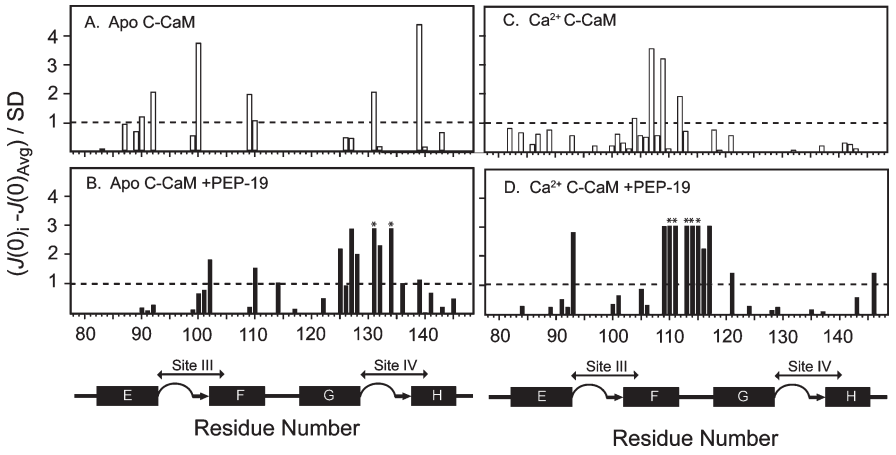

FIGURE 7: Identification of residues exhibiting conformational exchange on the microsecond to millisecond time scale in PEP-19-bound apo C-CaM and Ca^{2+}-C-CaM based on reduced spectral density mapping. Values on the *Y*-axis are calculated as $[J(0)_i - J(0)_{avg}]/SD$. Residues for which $[J(0)_i - J(0)_{avg}]/SD > 1.0$ are considered to undergo significant chemical and conformational exchange. Asterisks indicate residues with extreme line broadening.

DISCUSSION

Calmodulin is an essential and versatile Ca^{2+} sensor capable of interacting with numerous target proteins; however, its intrinsic biochemical properties become limiting in cells that have very rapid Ca^{2+} oscillations, high total Ca^{2+} levels, numerous CaM binding proteins, and limiting levels of CaM. This explains the need for proteins that can act as regulators of CaM signaling, or RCS proteins, to allow CaM to respond to diverse Ca^{2+} signals and achieve its wide array of known activities. We showed that the small neuronal IQ motif proteins PEP-19 (62 amino acids) and RC3 (78 amino acids) modulate the Ca^{2+} binding properties of CaM (*12*, *38*). Another small neuronal protein called ARPP-21 (88 amino acids) was shown to inhibit the binding of CaM to target proteins (*39*). These activities could exert broad effects on cell activities. Indeed, ARPP-21 regulates Ca^{2+} channel activity in mammalian brain, and RC3 plays a role in learning and memory (*39*−*45*). PEP-19 is thought to have cytoprotective activity on the basis of its pattern of expression in cells that are affected by Alzheimer's (*6*) and Huntington's diseases (*7*), and expression of PEP-19 inhibits apoptosis and cell death due to Ca^{2+} overload (*8*, *9*). PEP-19 is of particular interest because it is expressed in non-neuronal tissues, including endocrine, reproductive, and urinary organs that have highly active Ca^{2+} dynamics (*46*).

Diverse effects on essential cellular activities highlight the biological significance of PEP-19, ARPP-21, and RC3, and the need to understand their mechanisms of action. We showed previously that PEP-19 greatly increased the k_{on} and k_{off} rates for the binding of Ca^{2+} to the C-domain of CaM, with no change in apparent Ca^{2+} binding affinity (*12*), and that it decreased the cooperativity of Ca^{2+} binding (*14*). Changes in the cooperativity and kinetics of Ca^{2+} binding could result from static or dynamic properties of the CaM−PEP-19 complex. Dynamic properties are of particular interest because it is well-known that protein motions on the microsecond to millisecond time scale are often coupled with protein function (*47*−*50*), and the rate of Ca^{2+} exchange in the C-domain of CaM is correlated with rates of protein conformational exchange (*15*, *18*, *51*). The disordered nature of PEP-19 is significant because it could form so-called "fuzzy" complexes (*52*), in which bound PEP-19 remains partially disordered to induce conformational exchange in CaM, and because disordered regions in proteins have been shown to enhance allosteric effects (*53*). These relationships led us to characterize the effect of PEP-19 on backbone dynamics of C-CaM and to provide the experimental evidence for changes in cooperative Ca^{2+} binding at the atomic level.

It is well established that the C-domain of CaM binds two Ca^{2+} ions with a high degree of cooperativity (*12*, *31*, *54*−*56*). Figure 3 shows that this cooperativity results in the apparent slow exchange of amide resonances during titration with Ca^{2+} such that cross-peaks for only the zero-Ca^{2+} and two-Ca^{2+} forms are observed at all Ca^{2+}:C-CaM ratios. In contrast, intermediate exchange is observed when C-CaM is titrated with Ca^{2+} in the presence of PEP-19, resulting in severe broadening of most amide cross-peaks at intermediate Ca^{2+} levels. Amides for residues in the linker region between Ca^{2+} binding sites III and IV and near the N- and C-termini are observed at lower contour levels at all Ca^{2+}:C-CaM ratios, and many of these residues, including Thr117 shown in Figure 4, exhibit a shift in the direction of the resonance migration at $[Ca^{2+}]/[C\text{-CaM}]$ ratios of >1.0. The simplest explanation for this is that PEP-19 decreases the cooperativity of binding of Ca^{2+} to C-CaM, which allows a significant population of the one-Ca^{2+} form of the C-CaM−PEP-19 complex to accumulate at low Ca^{2+} levels. The effects of Ca^{2+} on amide cross-peaks for Gly98 in Ca^{2+} binding site III and Gly134 in Ca^{2+} binding site IV indicate that Ca^{2+} binds preferentially to site IV in the presence of PEP-19. This Ca^{2+} binding preference is generally consistent with Malmendal et al. (*15*), who concluded that Ca^{2+} binds preferentially to site IV of unmodified free CaM at very low Ca^{2+} levels. Decreased cooperativity may be intrinsically linked to the effects of PEP-19 on Ca^{2+} k_{on} and k_{off} rates based on a mathematical model in which binding of the first Ca^{2+} ion to either site III or IV is characterized by fast rate constants, while binding the second Ca^{2+} occurs with much slower rates due to cooperative effects (*14*). This implies that attenuation of cooperativity by PEP-19 will increase Ca^{2+} binding rate constants by allowing stronger expression of rapid rates associated with independent binding to site III or IV.

We used several criteria to identify residues in apo and Ca^{2+}-bound C-CaM that experience conformational and chemical exchange (R_{ex}) in the presence or absence of PEP-19. Residues indicated by bold lettering in Table 2 are those that experience severe exchange broadening or that show significant conformational exchange based on high $J(0)$ values from reduced spectral density mapping, as well as high values for R_2/R_1 and R_1R_2. Figure 8A shows that residues with significant R_{ex} in apo C-CaM

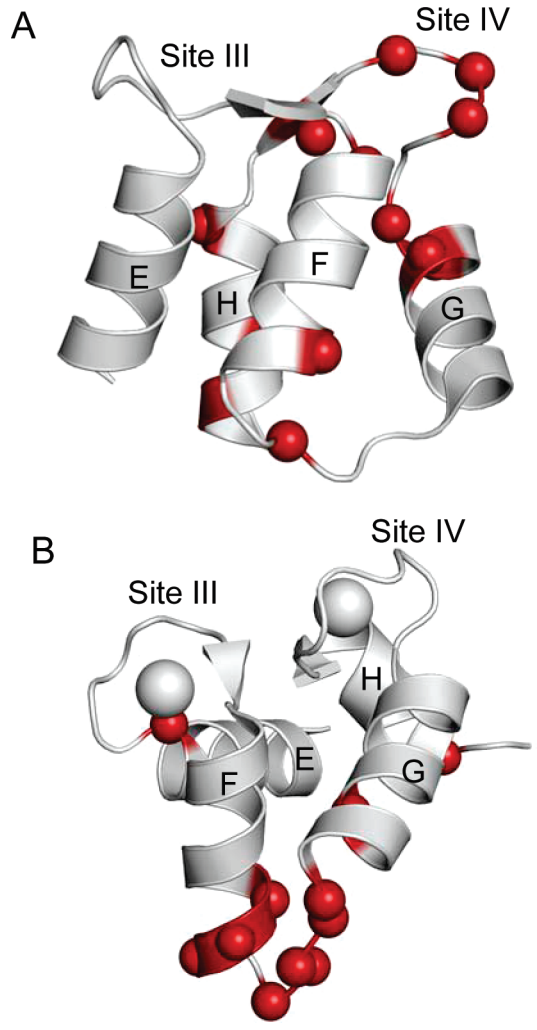

FIGURE 8: Summary of residues that exhibit significant conformational exchange for apo and Ca^{2+}-bound C-CaM in the presence of PEP-19. Panels A and B show the NMR solution structures for apo (PDB entry 1F71) and Ca^{2+}-bound forms of C-CaM (PDB entry 1J7P), respectively. Colored balls indicate residues that exhibit significant conformational exchange and are shown in lettering in Table 2.

bound to PEP-19 are localized to Ca^{2+}-binding loop IV and the short β-strands between loops III and IV. In contrast, Figure 8B shows that residues 109−117 in helix F and the linker between helices F and G of Ca^{2+}-C-CaM show conformational exchange in the presence of PEP-19. This pattern of residues with R_{ex} differs from the effect of a peptide from transcription factor SEF2-1, which induces R_{ex} primarily in residues 142−147 at the C-terminus of Ca^{2+}-CaM (*57*). It also differs from the effect of binding of a CaMKI peptide to Ca^{2+}-CaM, which causes relatively small R_{ex} in residues 102, 105−107, and 109 (*58*).

The pattern of residues with R_{ex}, and the k_{on} and k_{off} rates for binding of PEP-19 to CaM, suggest that conformational exchange is derived from different mechanisms for apo and Ca^{2+}-bound C-CaM. Residues with R_{ex} in the apo C-CaM−PEP-19 complex are primarily localized to Ca^{2+} binding site IV; however, this does not correspond to the PEP-19 binding site, which is localized primarily to residues 108−117 on the basis of amide chemical shift mapping shown in Figure 1. This suggests that R_{ex} is not due to intermolecular chemical exchange between apo C-CaM and PEP-19, but to intramolecular conformational exchange within the apo CaM−PEP-19 complex. This is consistent with k_{on} and k_{off} rates of 1 μM^{-1} s^{-1} and 5.6 s^{-1}, respectively, for binding of PEP-19 to apo CaM (*13*). Under conditions used for relaxation measurements, these rates give an estimated k_{ex} for intermolecular chemical exchange of ~200 s^{-1}, which is at the limit of the time frame that would give rise to R_{ex}. On the other hand, k_{on} and k_{off} rates for binding of PEP-19 to Ca^{2+}-CaM are least 20 μM^{-1} s^{-1} and 400 s^{-1}, respectively (*13*). These rates give a k_{ex} of least 4500 s^{-1}, which is well within the range that would give rise to R_{ex}. In addition, residues with R_{ex} in the Ca^{2+}-C-CaM−PEP-19 complex are localized to the PEP-19 binding site. This suggests that conformational exchange induced by PEP-19 in Ca^{2+}-bound C-CaM is due to intermolecular chemical exchange.

The effects of PEP-19 on the cooperativity and k_{on} and k_{off} rates of binding of Ca^{2+} to CaM may involve residues that experience conformational exchange on the slow time scale. The structural basis for cooperativity of Ca^{2+} binding is primarily associated with two structural features of paired EF hands. The first is the antiparallel β-sheet formed between short β-strands in Ca^{2+} binding sites III and IV. This structure is also formed in other paired EF-hands and was proposed as a conduit that transmits structural changes between Ca^{2+} binding sites in calbindin D_{9k} (*59*). Residues in the β-sheet region of apo C-CaM, but not Ca^{2+}-C-CaM, show increased R_{ex} when bound to PEP-19, including Ala102 in the strand−helix junction of Ca^{2+} binding loop III, and a cluster of residues across EF-hand IV. This supports a model in which PEP-19 increases the Ca^{2+} k_{on} rate by inducing conformational fluctuations in regions that lead to decreased Ca^{2+} binding cooperativity and preferential binding of Ca^{2+} to site IV. The second structural feature is the polypeptide linker between helix F of Ca^{2+}-binding site III and helix G in site IV of CaM. This strong covalent coupling would transmit conformational changes when the first Ca^{2+} binds to either site III or IV (*60*). PEP-19 induces R_{ex} for residues in this region of Ca^{2+}-bound but not apo C-CaM, which may reflect coupling between protein dynamics and the Ca^{2+} k_{off} rate. Another potential mechanism for increasing the Ca^{2+} k_{off} rate involves Asp93, which has increased R_{ex} in Ca^{2+}-bound C-CaM in the presence of PEP-19. The side chain carboxyl group of Asp93 contributes the $+X$ ligand for coordination of Ca^{2+} at site III and also forms a hydrogen bond with Phe89 (Asp93 H_N → Phe89 C′) (*61*) that stabilizes the otherwise unfavorable proximity of the negatively charged oxygen atoms in the coordination sphere of the bound Ca^{2+}. Conformational exchange at Asp93 in the presence of PEP-19 may increase the Ca^{2+} k_{off} rate.

In summary, the results presented here fill a gap in our understanding of how binding to proteins affects dynamic processes in CaM, by characterizing the effects of an intact, intrinsically disordered protein that binds with relatively low affinity but selectively to the C-domain of CaM in the presence or absence of Ca^{2+}. Binding of PEP-19 has no effect on CaM backbone dynamics on the fast nanosecond to picosecond time scale but increases conformational exchange on the slow microsecond to millisecond time scale, and patterns of residues that exhibit conformational exchange differ significantly for apo versus Ca^{2+}-bound CaM. The data provide structural and dynamic evidence to support models in which PEP-19 decreases the degree of Ca^{2+} binding cooperativity in the C-domain of CaM and accelerates Ca^{2+} k_{on} and k_{off} rates with no change in the apparent Ca^{2+} binding affinity.

SUPPORTING INFORMATION AVAILABLE

Comparison of secondary structures for the C-domain of free and PEP-19-bound CaM (Table 1), binding PEP-19 to apo CaM

that causes significant resonance line broadening for residues in the C-domain (Figure 1), comparison of $^{1}H-^{15}N$ HSQC spectra of C-CaM and intact CaM in the absence and presence of Ca^{2+} (Figure 2), plot of amide chemical shift differences ($\Delta\delta_{avg}$) as a function of residue number for C-CaM and the C-domain of intact CaM in the absence and presence of Ca^{2+} (Figure 3), comparison of $^{1}H-^{15}N$ HSQC spectra of Ca^{2+}-bound C-CaM and intact Ca^{2+}-bound CaM in the presence of excess PEP-19 at 298 K (Figure 4), structural perturbations of C-CaM induced by PEP-19 binding at 298 K (Figure 5), and identification of secondary structures for the Ca^{2+}-bound intact CaM−PEP-19 complex (Figure 6). This material is available free of charge via the Internet at http://pubs.acs.org.

REFERENCES

1. Rhoads, A., and Bahler, M. (2002) Calmodulin signaling via the IQ motif. *FEBS Lett. 513*, 107–113.
2. Gerendasy, D. D. (1999) Homeostatic tuning of the Ca^{2+} signal transduction by members of the calpacitin protein family. *J. Neurosci. Res. 58*, 107–119.
3. Reck-Peterson, S. L., Provance, W. D. J., Mooseker, M. S., and Mercer, J. A. (2000) Class V myosins. *Biochim. Biophys. Acta 1496*, 36–51.
4. Jurado, L. A., Sethu, P., Chockalingam, P. S., and Jarrett, H. W. (1999) Apocalmodulin. *Physiol. Rev. 79*, 661–681.
5. Hartmann, J., and Konnerth, A. (2005) Determinants of postsynaptic Ca^{2+} signaling in Purkinje neurons. *Cell Calcium 37*, 459–466.
6. Slemmon, J. R., Feng, B., and Erhardt, J. A. (2000) Small proteins that modulate calmodulin-dependent signal transduction: Effects of PEP-19, neuromodulin, and neurogranin on enzyme activation and cellular homeostasis. *Mol. Neurobiol. 22*, 99–113.
7. Utal, A. K., Stopka, A. L., Roy, M., and Coleman, P. D. (1998) PEP-19 immunohistochemistry defines the basal ganglia and associated structures in the adult human brain, and is dramatically reduced in Huntington's disease. *Neuroscience 86*, 1055–1063.
8. Erhardt, J. A., Legos, J. J., Johanson, R. A., Slemmon, J. R., and Wang, X. (2000) Expression of PEP-19 inhibits apoptosis in PC12 cells. *NeuroReport 11*, 3719–3323.
9. Kanazawa, Y., Makino, M., Morishima, Y., Yamada, K., Nabeshima, T., and Shirakaki, Y. (2008) Degradation of PEP-19 calmodulin-binding protein by calpain is implicated in neuronal cell death induced by intracellular Ca^{2+} overload. *Neuroscience 154*, 473–481.
10. Kanamori, T., Takakura, K., Mandai, M., Kariya, M., Fukuhara, K., Kusakari, T., Momma, C., Shime, H., Yagi, H., Konishi, M., Suzuki, A., Matsumura, N., Nanbu, K., Fujuita, N., and Fujii, S. (2003) PEP-19 overexpression in human uterine leiomyoma. *Mol. Hum. Reprod. 9*, 709–717.
11. Ross, D. T.; et al. (2000) Systematic variation in gene expression in human cancer cell lines. *Nat. Genet. 24*, 208–209.
12. Putkey, J. A., Kleerekoper, Q., Gaertner, T. R., and Waxham, M. N. (2003) A new role for IQ motif proteins in regulating calmodulin function. *J. Biol. Chem. 278*, 49667–49670.
13. Kleerekoper, Q., and Putkey, J. A. (2009) PEP-19: An instrinsically disordered regulator of CaM signaling. *J. Biol. Chem. 284*, 7455–7464.
14. Putkey, J. A., Waxham, M. N., Gaertner, T. A., Brewer, K. J., Goldsmith, M., Kubota, Y., and Kleerekoper, Q. K. (2008) Acidic/IQ motif regulators of calmodulin. *J. Biol. Chem. 283*, 1401–1410.
15. Malmendal, A., Evenas, J., Forsen, S., and Akke, M. (1999) Structural dynamics in the C-terminal domain of calmodulin at low calcium levels. *J. Mol. Biol. 293*, 883–899.
16. Zhang, M., Tanaka, T., and Ikura, M. (1995) Calcium-induced conformational transition revealed by the solution structure of apo-calmodulin. *Nat. Struct. Biol. 2*, 758–767.
17. Tjandra, N., Kuboniwa, H., Ren, H., and Bax, A. (1995) Rotational dynamics of calcium-free calmodulin studieed by ^{15}N-NMR relaxation measurements. *Eur. J. Biochem. 230*, 1014–1024.
18. Evenas, J., Malmendal, A., and Akke, M. (2001) Dynamics of the transition between open and closed conformations in a calmodulin C-terminal domain mutant. *Structure 9*, 185–195.
19. Peersen, O. B., Madsen, T. S., and Falke, J. J. (1997) Intermolecular tuning of calmodulin by target peptides and proteins: Differential effects on Ca^{2+} binding and implications for kinase activation. *Protein Sci. 6*, 794–807.
20. Putkey, J. A., Slaughter, G. R., and Means, A. R. (1985) Bacterial expression and characterization of proteins derived from the chicken calmodulin cDNA and a calmodulin processed gene. *J. Biol. Chem. 260*, 4704–4712.
21. Putkey, J. A., and Waxham, M. N. (1996) A peptide model for calmodlin trapping by calcium/calmodulin-dependent protein kinase II. *J. Biol. Chem. 271*, 29619–29623.
22. Xiong, L. W., Kleerekoper, Q. K., Wang, X., and Putkey, J. A. (2010) Intra- and interdomain effects due to mutation of calcium-binding sites in calmodulin. *J. Biol. Chem. 285*, 8094–8103.
23. Farrow, N. A. R., Muhandiram, R., Singer, A. U., Pascal, S. M., Kay, C. M., Gish, G., Shoelson, S. E., Pawson, T., Forman-Kay, J. D., and Kay, L. E. (1994) Backbone dynamics of a free and phosphopeptide-complexed Src homology 2 domain studied by ^{15}N NMR relaxation. *Biochemistry 33*, 5984–6003.
24. Wishart, D. S., Bigam, C. G., Yao, J., Abildgaard, F., Dyson, H. J., Oldfield, E., Markley, J. L., and Sykes, B. D. (1995) H-1, C-13 and N-15 Chemical-Shift Referencing in Biomolecular Nmr. *J. Biomol. NMR 6*, 135–140.
25. Farrow, N. A., Zhang, O., Szabo, A., Torchia, D. A., and Kay, L. E. (1995) Spectral density function mapping using ^{15}N relaxation data exclusively. *J. Biomol. NMR 6*, 153–162.
26. Sahu, S. C., Bhuyan, A. K., Majumdar, A., and Udgaonkar, J. B. (2000) Backbone dynamics of barstar: A ^{15}N NMR relaxation study. *Proteins 41*, 460–474.
27. Kay, L. E., Torchia, D. A., and Bax, A. (1989) Backbone Dynamics of Proteins as Studied by ^{15}N Inverse Detected Heteronuclear NMR Spectroscopy: Application to Staphylococcal Nuclease. *Biochemistry 28*, 8972–8979.
28. Mercier, P., Spyracopoulos, L., and Sykes, B. D. (2001) Structure, dynamics, and thermodynamics of the structural domain of troponin C in complex with the regulatory peptide 1−40 of troponin I. *Biochemistry 40*, 10063–10077.
29. Evans, T. I., and Shea, M. A. (2009) Energetics of calmodulin domain interactions with the calmodulin binding domain of CaMKII. *Proteins 76*, 47–61.
30. VanScyoc, W. S., Sorensen, B. R., Rusinova, E., Laws, W. R., Ross, J. B., and Shea, M. A. (2002) Calcium binding to calmodulin mutants monitored by domain-specific intrinsic phenylalanine and tyrosine fluorescence. *Biophys. J. 83*, 2767–2780.
31. Linse, S., Helmersson, A., and Forsén, S. (1991) Calcium binding to calmodulin and its globular domains. *J. Biol. Chem. 266*, 8050–8054.
32. Bayley, P. M., Findlay, W. A., and Martin, S. R. (1996) Target recognition by calmodulin: Dissecting the kinetics and affinity of interaction using short peptide sequences. *Protein Sci. 5*, 1215–1228.
33. Strynadka, N. C., and James, M. N. (1989) Crystal structures of the helix-loop-helix calcium-binding proteins. *Annu. Rev. Biochem. 58*, 951–998.
34. Barbato, G., Ikura, M., Kay, L. E., Pastor, R. W., and Bax, A. (1992) Backbone dynamics of calmodulin studied by ^{15}N relaxation using inverse detected two-dimensional NMR spectroscopy: The central helix is flexible. *Biochemistry 31*, 5269–5278.
35. Clore, G. M., Driscoll, P. C., Wingfield, P. T., and Gronenborn, A. M. (1990) Analysis of the backbone dynamics of interleukin-1β using two-dimensional inverse detected heteronuclear ^{15}N-^{1}H NMR spectroscopy. *Biochemistry 29*, 7387–7401.
36. Baudier, J., Deloulme, J. C., Van Dorsselaer, A., Black, D., and Matthes, H. W. (1991) Purification and characterization of a brain-specific protein kinase C substrate, neurogranin (p17). Identification of a consensus amino acid sequence between neurogranin and neuromodulin (GAP43) that corresponds to the protein kinase C phosphorylation site and the calmodulin-binding domain. *J. Biol. Chem. 266*, 229–237.
37. Peng, J. W., and Wagner, G. (1995) Frequency spectrum of NH bonds in eglin c from spectral density mapping at multiple fields. *Biochemistry 34*, 16733–16752.
38. Gaertner, T. R., Putkey, J., and Waxham, M. N. (2002) Kinetics of calmodulin binding to RC3/neurogranin. *Soc. Neurosci. Abstr.,* 30.
39. Rakhilin, S. V., Olson, P. A., Nishi, A., Starkove, N. N., Fienberg, A. A., Nairn, A. C., Surmeier, D. J., and Greengard, P. (2004) A network of control mediated by regulator of calcium/calmodulin-dependent signaling. *Science 306*, 698–701.
40. Miyakawa, T., Yared, E., Pak, J. H., Huang, F. L., Huang, K.-P., and Crawley, J. N. (2001) Neurogranin null mutant mice display performance deficits on spatial learning tasks with anxiety related components. *Hippocampus 11*, 763–775.
41. Wu, J., Li, L., Huang, K.-P., and Huang, F. L. (2002) Attenuation of protein kinase C and cAMP-dependent protein kinase signal transduction in the neurogranin knockout mouse. *J. Biol. Chem. 277*, 19498–19505.
42. Krucker, T., Siggins, G. R., McNamara, R. K., Lindsley, K. A., Dao, A., Allison, D. W., De Lecea, L., Lovenberg, T. W., Sutcliffe, J. G.,

and Gerendasy, D. D. (2002) Targeted disruption of RC3 reveals a calmodulin-based mechanism for regulating metaplasticity in the hippocampus. *J. Neurosci. 22*, 5525–5535.
43. Englander, W. S. (2000) Protein folding intermediates and pathways studied by hydrogen exchange. *Annu. Rev. Biomol. Struct. 29*, 213–238.
44. Pak, J. H., Huang, F. L., Li, J., Balschun, D., Reymann, K. G., Chiang, C., Westphal, H., and Huang, K.-P. (2000) Involvement of neurogranin in the modulation of calcium/calmodulin-dependent protein kinase II, synaptic plasticity, and spatial learning: A study with knockout mice. *Proc. Natl. Acad. Sci. U.S.A. 97*, 11232–11237.
45. Huang, F. L., Huang, K. P., Wu, J., and Boucheron, C. (2006) Environmental enrichment enhances neurogranin expression and hippocampal learning and memory but fails to rescue the impairments of neurogranin null mutant mice. *J. Neurosci. 26*, 6230–6237.
46. Ge, X., Yamamoto, S., Tsutsumi, S., Midorikawa, Y., Ihara, S., Wang, S. M., and Aburatani, H. (2005) Interpreting expression profiles of cancers by genome-wide survey of breadth of expression in normal tissues. *Genomics 86*, 127–141.
47. Palmer, A. G., Kroenke, C. D., and Loria, J. P. (2001) Nuclear magnetic resonance methods for quantifying microsecond-to-millisecond motions in biological macromolecules. *Methods Enzymol. 339*, 204–238.
48. Mittermaier, A., and Kay, L. E. (2006) New tools provide new insights in NMR studies of protein dynamics. *Science 312*, 224–228.
49. Boehr, D. D., Dyson, H. J., and Wright, P. E. (2006) An NMR perspective on enzyme dynamics. *Chem. Rev. 106*, 3055–3079.
50. Kern, D., Eisenmesser, E. Z., and Wolf-Watz, M. (2005) Enzyme dynamics during catalysis measured by NMR spectroscopy. *Methods Enzymol. 394*, 507–524.
51. Evenas, J., Forsen, S., Malmendal, A., and Akke, M. (1999) Backbone dynamics and energetics of a calmodulin domain mutant exchanging between closed and open conformations. *J. Mol. Biol. 289*, 603–617.
52. Tompa, P., and Fuxreiter, M. (2008) Fuzzy complexes: Polymorphism and structural disorder in protein-protein interactions. *Trends Biochem. Sci. 33*, 2–8.
53. Hilser, V. J., and Thompson, E. B. (2007) Intrinsic disorder as a mechanism to optimize allosteric coupling in proteins. *Proc. Natl. Acad. Sci. U.S.A. 104*, 8311–8315.
54. Biekofsky, R. R., Martin, S. R., Browne, J. P., Bayley, P. M., and Feeney, J. (1998) Ca^{2+} coodination to backbone carbonyl oxygen atoms in calmodulin and other EF-hand proteins: ^{15}N chemical shifts as probes for monitoring individual-site Ca^{2+} coodination. *Biochemistry 37*, 7617–7629.
55. Pedigo, S., and Shea, M. A. (1995) Discontinuous equilibrium titrations of cooperative calcium binding to calmodulin monitored by 1-D ^{1}H-nuclear magnetic resonance spectroscopy. *Biochemistry 34*, 10676–10689.
56. Crouch, T. H., and Klee, C. B. (1980) Positive cooperative binding of calcium to bovine brain calmodulin. *Biochemistry 19*, 3692–3698.
57. Larsson, G., Schleucher, J., Onions, J., Hermann, S., Grundstrom, T., and Wijmenga, S. S. (2005) Backbone dynamics of a symmetric calmodulin dimer in complex with the calmodulin-binding domain of the basic-helix-loop-helix transcription factor SEF2-1/E2-2: A highly dynamic complex. *Biophys. J. 89*, 1214–1226.
58. Frederick, K. K., Kranz, J. K., and Wand, A. J. (2006) Characterization of the backbone and side chain dynamics of the CaM-CaMKIp complex reveals microscopic contributions to protein conformational entropy. *Biochemistry 45*, 9841–9848.
59. Nelson, M. R., Thulin, E., Fagan, P. A., Forsen, S., and Chazin, W. J. (2002) The EF-hand domain: A globally cooperative structural unit. *Protein Sci. 11*, 198–205.
60. Gifford, J. L., Walsh, M. P., and Vogel, H. J. (2007) Structures and metal-ion-binding properties of the Ca^{2+}-binding helix-loop-helix EF-hand motifs. *Biochem. J. 405*, 199–221.
61. Juranic, N., Atanasova, E., Streiff, J. H., Macura, S., and Prendergast, F. G. (2007) Solvent-induced differentiation of protein backbone hydrogen bonds in calmodulin. *Protein Sci. 16*, 1329–1337.